Received 11 June 2019; revised 12 August 2019 and 25 September 2019; accepted 10 October 2019. Date of publication 15 October 2019; date of current version 6 December 2019. The review of this article was arranged by Editor H. T. E. Teo.

Digital Object Identifier 10.1109/JEDS.2019.2947246

Processing-Structure-Protrusion Relationship of 3-D Cu TSVs: Control at the Atomic Scale

JINXIN LIU[1], ZHIHENG HUANG[1], PAUL P. CONWAY[2], AND YANG LIU[3]

1 School of Materials Science and Engineering, Sun Yat-sen University, Guangzhou 510275, China
2 School of Mechanical, Electrical and Manufacturing Engineering, Loughborough University, Loughborough LE11 3TU, U.K.
3 School of Electronics and Information Technology, Sun Yat-sen University, Guangzhou 510006, China

CORRESPONDING AUTHOR: Z. HUANG (e-mail: hzh29@mail.sysu.edu.cn)

This work was supported in part by the National Natural Science Foundation of China under Grant 51832002, in part by the Guangdong Natural Science Foundation under Grant 2015A030312011, in part by the Zhuhai Key Technology Laboratory of Wide Bandgap Semiconductor Power Electronics under Grant 20167612042080001, and in part by the Zhuhai Rossini Watch Industry Ltd. under Grant 29000-71010006.

ABSTRACT A phase-field-crystal model is used to investigate the processing-structure-protrusion relationship of blind Cu through-silicon vias (TSVs) at the atomic scale. A higher temperature results in a larger TSV protrusion. Deformation via dislocation motion dominates at temperatures lower than around 300°C, while both diffusional and dislocation creep occur at temperatures greater than around 300°C. TSVs with smaller sidewall roughness R_a and wavelength λ_a exhibit larger protrusions. Moreover, different protrusion profiles are observed for TSVs with different grain structures. Both protrusions and intrusions are observed when a single grain is placed near the TSV top end, while the top surface protrudes near both edges when it contains more grains. Under symmetric loading, coalescence of the grains occurs near the top end, and a symmetric grain structure can accelerate this process. The strain distributions in TSVs are calculated, and the eigenstrain projection along the vertical direction can be considered an index to predict the TSV protrusion tendency.

INDEX TERMS Copper, interconnections, reliability modeling, through-silicon via, microstructure.

I. INTRODUCTION

Three-dimensional (3D) devices, e.g., stacked high bandwidth memory (HBM) [1], are expected to be developed to keep up with the increasing package density requirements. In realizing 3D packaging, an important idea is to utilize through-silicon via (TSV) technology [2]–[4]. However, the mismatch of the thermal expansion coefficients between the normal filler material Cu and the surrounding silicon frequently leads to protrusion when the TSV structures are subjected to thermal processing [5]. This protrusion causes damage to the back-end-of-line (BEoL) layers and thus failure of 3D packaging, posing a serious reliability issue to be solved.

When investigating Cu TSV protrusion, temperature is an important processing parameter. Heryanto *et al.* reported that the hardness, yield strength, and elastic modulus of Cu in TSVs decreased when the samples were annealed at higher temperatures [6]. X-ray microbeam diffraction was used by Jiang *et al.* to measure the Cu deformation under different thermal cycles from room temperature to 200°C, 300°C, and 400°C [7]. In TSV fabrication, the surface of the drilled via cannot be controlled to be perfectly flat, and therefore, sidewall scalloping roughness exists [3]. Ehsan *et al.* emphasized that the TSV sidewall roughness is a paramount factor that governs the electrical performance, and can lead to a significant amount of leakage current, therefore impacting the capacitance, resistance and inductance [8]. Nakamura *et al.* reported that a tensile stress as high as 340 MPa is generated at the groove points on a rough sidewall [9]. The stress concentration at these locations may influence the protrusion behavior. Furthermore, the microstructure of polycrystalline Cu in TSVs also needs to be considered to clarify the origin of Cu protrusion. For example, the electron backscattered diffraction (EBSD) technique was used by Jiang *et al.* to show that larger grains are present in TSVs after thermal cycling with a higher peak temperature [10]. Recently, a

statistical model correlating the protrusion height and the number of grains near the TSV top end was established by Messemaeker *et al.* [11]. Optimized electroplating and postplating annealing processing of TSVs were reported to possibly lead to a stabilized microstructure, which relieved the via protrusion [12]. However, the behavior of TSV protrusion is complex and a combined result of the processing parameters, e.g., temperature, and the sidewall roughness, microstructure and strain or stress state in TSVs. Synchrotron X-ray microdiffraction was carried out by Liu *et al.* for in situ measurement of microscale thermomechanical strain [13]. Okoro *et al.* measured stresses in TSVs of different sizes using micro-Raman spectroscopy [14].

To assist the understanding of the protrusion, controllable simulations considering atomic-scale structures can provide more direct information. In recent works, we used a phase-field-crystal (PFC) model to reproduce the process of Cu protrusion [15]–[17]. PFC models can reveal microstructural evolution in materials with atomic spatial scale and diffusive time scale resolutions, such as polycrystalline solidification, structural phase transformations, and heteroepitaxial growth [18], [19]. Moreover, the elasticity and plasticity phenomena of solid-state processes can be captured by PFC models, such as dislocation motion, creation and annihilation and creep [20], [21].

In this study, we use the PFC model to further investigate TSV protrusion by incorporating different processing parameters and grain structures and reveal their influence on the resulting protrusion behavior. The rest of the paper is organized as follows. First, the PFC model and the method to calculate the strain are briefly introduced. Second, the effects of temperature and TSV sidewall roughness on protrusion are discussed. Moreover, the protrusion behaviors of TSVs with different grain structures are investigated in detail. Finally, the strain distributions in the TSVs are extracted from the atom displacements and the relevance of strain to protrusion is studied.

II. METHOD

The principle of the PFC model for simulating the microstructural evolution of a material is briefly reviewed here. First, the lattice of a crystalline material is represented as an order parameter ρ in the PFC model. The order parameter has the form of a plane wave with the same periodicity as the lattice and represents the local time-averaged atomic density of the material system. Using a two-point correlation function, a two-mode PFC model was developed to simulate a square lattice in two dimensions, corresponding to the {100} crystallographic plane of Cu [22]. The two-mode order parameter ρ is written as follows [22]:

$$\rho = \bar{\rho} + A\big[\cos(qx) + \cos(qy)\big] + B\cos(qx)\cos(qy) \quad (1)$$

where A and B are related to the amplitudes of two sets of density waves and $q = 2\pi/a$ is related to the lattice constant a. Moreover, the symbol $a = 0.25$ nm is defined hereinafter as the lattice constant of Cu. Then, the free energy of the system is written as follows [22]:

$$F[\rho] = \int \mathrm{d}\boldsymbol{r}\left\{\frac{\rho}{2}\left[T + \left(\nabla^2 + 1\right)^2\left(\nabla^2 + Q^2\right)^2\right]\rho + \frac{\rho^4}{4}\right\} \quad (2)$$

where T is the scaling temperature and $Q^2 = 2$ is a constant. The microstructural evolution is obtained by solving the governing equation of the PFC model [22]:

$$\frac{\partial \rho}{\partial t} = \nabla^2 \frac{\delta F}{\delta \rho} \quad (3)$$

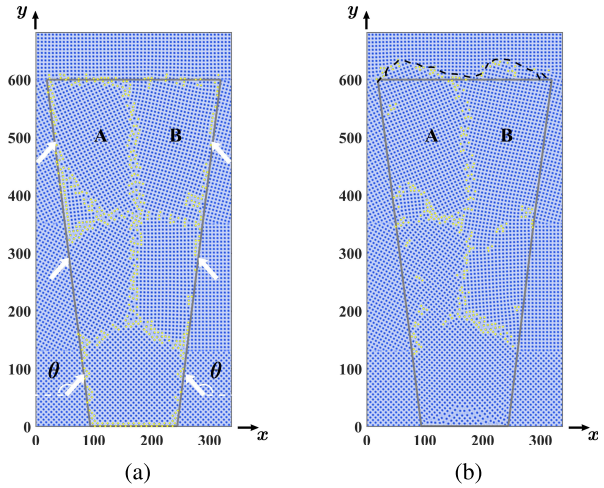

FIGURE 1. (a) Model configuration of a TSV structure. The edges of a trapezoidal TSV are outlined by solid gray lines. The parallel arrows indicate the direction of the loading applied to the TSV, which form an angle $\theta = 150°$ with the horizontal axis. (b) The black dashed curve outlines the protrusion profile at time $t = 30000$ during the loading stage. The defect atoms are highlighted by the yellow dots.

Fig. 1a shows the model configuration of our TSV structure. Here, a 2D PFC model is adopted for computational efficiency. Note that the TSV is a blind via in this study. The solid gray lines delineate the edges of the TSV, showing a trapezoidal TSV. Solid external layers are added around the TSV to facilitate the application of loading. The top layer is set as a grain with a 0° orientation, providing a solid cover for the TSV. In the PFC model, loading is applied by introducing a "penalty term" to the free energy with the following form [23]:

$$F[\rho]' = F[\rho] + \int \mathrm{d}\boldsymbol{r} M(\boldsymbol{r})[\rho(\boldsymbol{r}, t) - \rho(\boldsymbol{r}(\boldsymbol{v}, r), t)] \quad (4)$$

where $M(\boldsymbol{r})$ is nonzero only in the external layers, except for the top cover layer. Driven by the "penalty term", the atoms inside the external layers are forced to move with a predetermined velocity $\boldsymbol{v}$ in the direction defined by the arrows in Fig. 1a, forming an angle θ with the horizontal axis. Note that $\theta = 150°$ is used in this study. The other parameters used in the PFC model are set as follows: $(T, \bar{\rho}, A, B, q, |\boldsymbol{v}|) = (0.073, 0.69, 0.19, 0.12, 1.0, 1.0 \times 10^{-4})$. The model parameters fix the system temperature to be approximately 400°C. In experimental work, Cu TSVs are usually annealed at

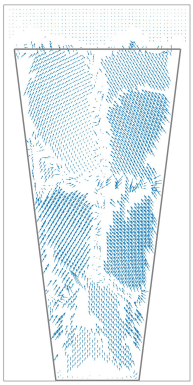

FIGURE 2. Example of the displacement map $\boldsymbol{u}(\boldsymbol{r})$ of a TSV structure, constructed by connecting the initial position of an atom at $t = 0$ to its corresponding position at $t = 30000$ during the loading stage.

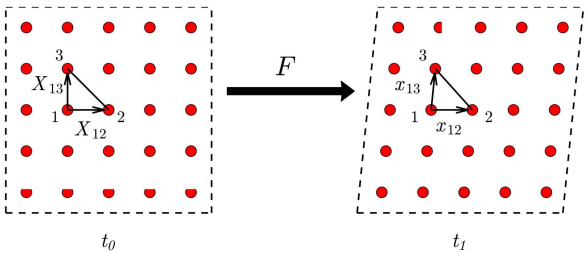

FIGURE 3. Schematic of the calculation of the deformation gradient $\boldsymbol{L}$. The vector $\boldsymbol{X_{12}}$ connects the 1^{st} and 2^{nd} vertices of a triangular element at $\boldsymbol{t_0}$, while $\boldsymbol{x_{12}}$ connects the same pair of atoms at the next time step $\boldsymbol{t_1}$.

$400-450$°C, resulting in Cu protrusion [6], [24], [25]. Note that the length and time scales in the original PFC model and this study are dimensionless. The length and time scales in the dimensionless PFC model can certainly be related to real dimension units. The lattice constant of Cu, i.e., $a = 0.25$ nm, can define the length scale. With respect to the time scale, it has been reported by Provatas and Heryanto that roughly 500 to 1000 time steps in the PFC model can simulate one diffusion time (e.g., 0.20 ms at 650°C) [26]. In addition, the atoms in or near the grain boundaries (GBs) and dislocations in the TSV are defined as defect atoms and are highlighted by the yellow dots in Fig. 1. More details are given in our previous study [16].

In the PFC model, the atoms are identified as the maxima of the order parameter $\rho(\boldsymbol{r}, t)$. The calculation of strain is based on the displacement of the atoms, i.e., the displacement $\boldsymbol{u}(\boldsymbol{r})$, which connects the positions of the same atom at two different time steps [27]. As an example, $\boldsymbol{u}(\boldsymbol{r})$ from $t = 0$ to $t = 30000$ is plotted in Fig. 2. To demonstrate how to calculate the strain, two schematic snapshots of a lattice at times t_0 and t_1 are taken, as shown in Fig. 3. The vector $\boldsymbol{X}_{mn} = \boldsymbol{X}_n - \boldsymbol{X}_m$ connects the m-th and n-th vertices of the triangular element at t_0, while $\boldsymbol{x}_{mn} = \boldsymbol{x}_n - \boldsymbol{x}_m$ connects the same pair of atoms at the next time step t_1. The deformation gradient F transforms such a triangular element from time t_0 to t_1, i.e., $\boldsymbol{x}_{mn} = L \cdot \boldsymbol{X}_{mn}$. Therefore, the deformation gradient

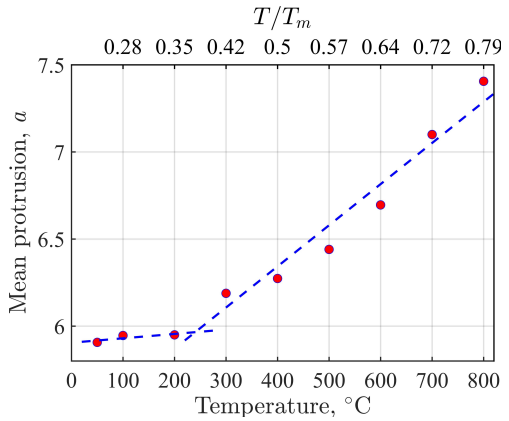

FIGURE 4. Plot of the mean protrusion height versus temperature. The grain structure and loading condition are defined in Fig. 1a.

F is related to the strain state by [27]:

$$L = \frac{\partial \boldsymbol{x}}{\partial \boldsymbol{X}} = I + \frac{\partial \boldsymbol{u}(\boldsymbol{r})}{\partial \boldsymbol{X}} \tag{5}$$

where I is the unit matrix. Finally, the strain components are obtained from L as follows: $\varepsilon_{xx} = L(1,1) - 1$, $\varepsilon_{yy} = L(2,2) - 1$, $\varepsilon_{xy} = L(1,2)$, and $\varepsilon_{yx} = L(2,1)$. The deformation field over the entire system can be written as a sum over all triangular elements [27]:

$$L_{macro} = \frac{\sum_i L_i V_i}{\sum_i V_i} \tag{6}$$

where V_i is the area of the triangular element in 2D.

III. RESULTS AND DISCUSSION

A. TEMPERATURE

Fig. 4 plots the protrusion height versus different temperatures. The protrusion height increases with increasing temperature. Different rates of increase exist in different temperature regimes, i.e., a lower rate for $T < 200$°C and a higher rate for $T > 300$°C. Different deformation mechanisms dominate in different temperature regimes. In the lower temperature range $T < 200$°C, only the dislocation motion causes the grains to deform under the applied loading. With an increase in temperature to 300°C and above, diffusional creep dominates, initiated by the GB diffusion, i.e., Coble creep, and successively activates lattice diffusion at approximately 600°C, i.e., Nabarro-Herring creep. Coble creep dominates at relatively lower temperatures, and a transition to Nabarro-Herring creep occurs as the temperature increases [28], [29]. Both the diffusional creep and dislocation creep contribute to the protrusion and lead to a larger protrusion under temperature $T > 300$°C. In addition, the atom diffusion and dislocation motion are faster at higher temperatures.

B. SIDEWALL ROUGHNESS

To investigate the effect of the sidewall roughness, a sinusoidal function, i.e., $y = A \cdot \sin(\frac{x}{N})$, is used to describe the

TABLE 1. Roughness parameters R_a and λ_a for models M1-M5 and protrusion statistics.

Model no.	R_a	λ_a	Mean protrusion (a)	Maximum protrusion (a)
M1	10	40π	4.5	7.6
M2	20	40π	3.9	6.6
M3	40	40π	3.6	6.3
M4	20	20π	4.0	8.4
M5	20	10π	4.4	8.8

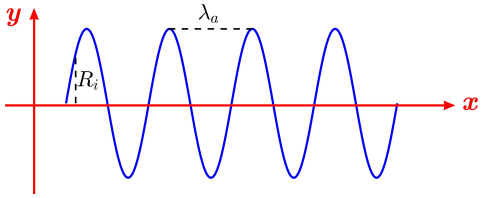

FIGURE 5. Illustration of the parameters R_i and λ_a characterizing the TSV sidewall roughness. The average roughness height R_a is obtained through the relationship $R_a = \frac{1}{L}\int_0^L |R_i(x)|dx$.

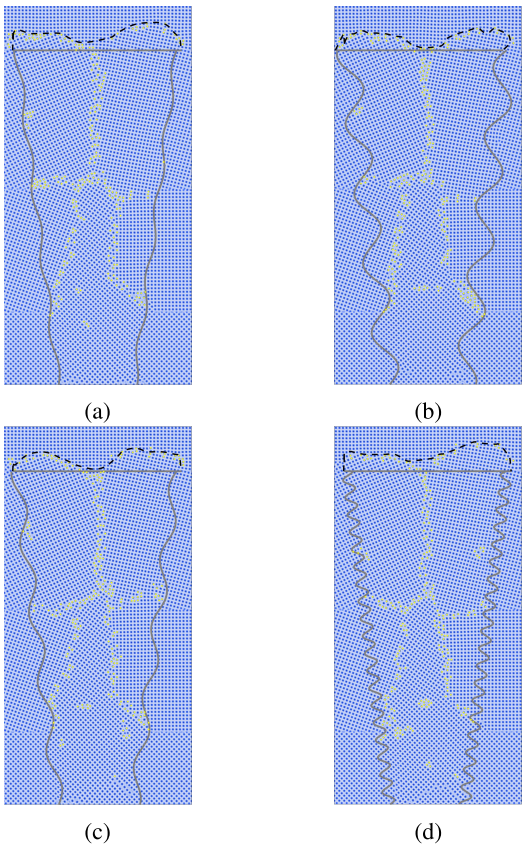

FIGURE 6. Protrusions of four TSVs with different sidewall roughness values: (a) M1, (b) M3, (c) M2 and (d) M5. The protrusion statistics are summarized in Table 1.

sidewall surface in our model, as shown in Fig. 5. Here, the roughness height is $R_a = 2 \cdot A$ and the average wavelength is $\lambda_a = 2\pi \cdot N$. Detailed model configurations and protrusion statistics are summarized in Table 1. Four models with different sidewall roughness values are shown in Fig. 6. Comparing M1 in Fig. 6a with M3 in Fig. 6b, a higher R_a will lead to a lower mean protrusion height because a higher R_a means larger grooves in the sidewall. The larger the grooves are, the more atoms and defects are impeded in their upward movement. As a result, a lower mean protrusion height can be expected. Considering M2 and M5, the mean protrusion height is larger with a smaller λ_a. A smaller λ_a indicates that more grooves exist in the sidewall. Despite more grooves impeding more atoms from moving, the effect of λ_a has been reported to be smaller than that of R_a: the roughness wavelength is only of secondary importance compared to the average roughness height [30]. On the other hand, dislocations are emitted from the groove points of the sidewall because of the stress concentration at these locations under the applied loading. More groove points mean that more dislocations may be emitted. When reaching the top surface, these emitted dislocations positively contribute to protrusion. In addition, the difference in the maximum protrusion heights between M2 and M5 is larger than that in the mean protrusion heights because more dislocations are emitted from the groove points of the sidewall in M5, thus contributing to the maximum protrusion height.

C. GRAIN STRUCTURE

Fig. 1 shows the protrusion of a TSV with two grains near the top end, and the protrusion profile is sketched by the black dashed curve, exhibiting two peaks directly produced by grains A and B. The simulation results suggest that the grains near the top end of the TSV, i.e., the grains adjacent to the top surface, directly contribute to both the protrusion profile and height. As shown in Fig. 7, the black curve in Fig. 7b highlighting the TSV with one grain near the top end exhibits both protrusion and intrusion behavior. For the TSV with four grains near the top end shown in Fig. 7c, Fig. 7d shows that the top surface protrudes near both edges, which is directly produced by grains A and D, and remains almost flat in the middle. Grains B and C produce little protrusion. Protrusion near both edges can also be found in the TSV with three grains near the top end, as shown in Fig. 8. The difference in the three-grain case lies in grain B in the middle, which forms a high angle GB with both grains A and C, shrinks with time and finally coalesces with the neighboring grains. For the four-grain case in Fig. 7d, although grains B and C also become smaller, the coalescence of grains proceeds much slower because the asymmetry of the grain structure impedes the motion of the triple junctions. Note the symmetry of the grain structure in Fig. 8. Due to the

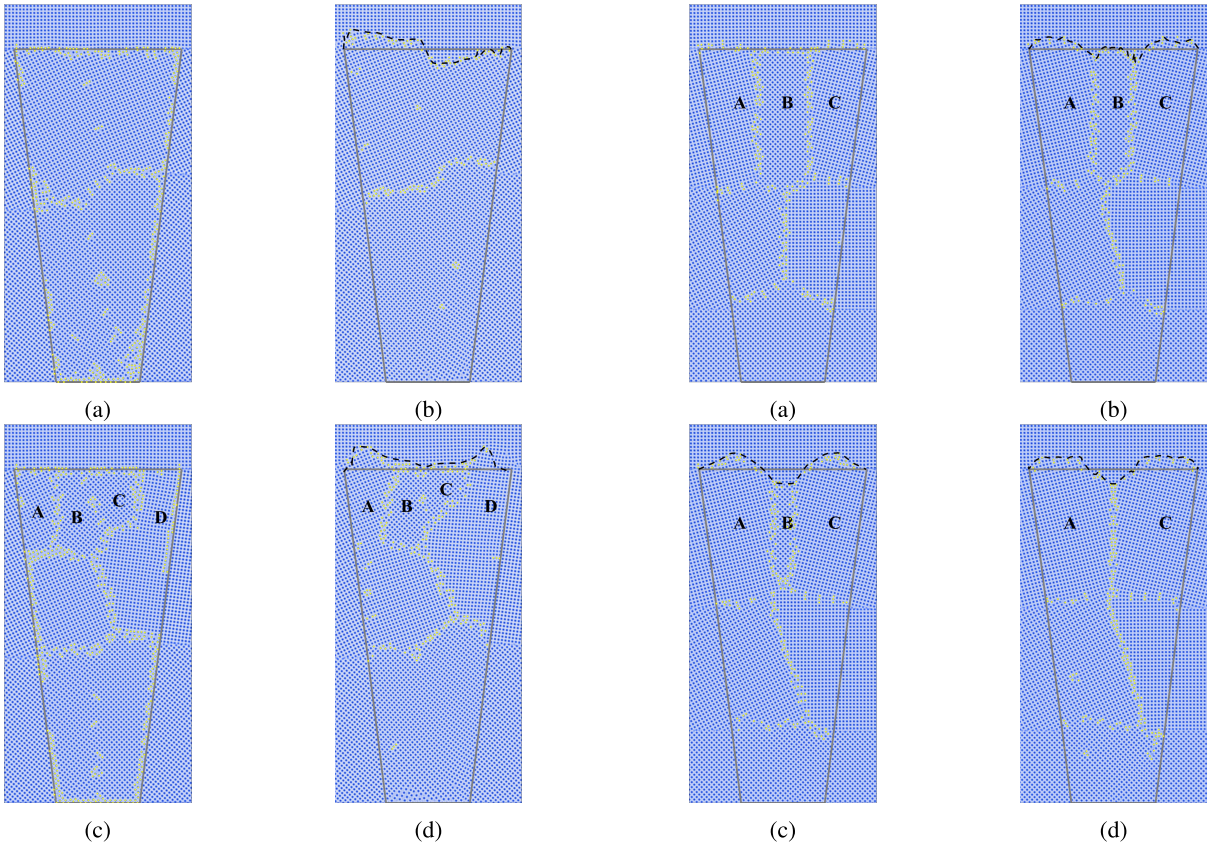

FIGURE 7. Protrusion profiles of two TSVs with different grain structures under the loading direction $\theta = 150°$. (a) $t = 0$ and (b) $t = 30000$, with a single grain placed near the top end; (c) $t = 0$ and (d) $t = 30000$, with four grains placed near the top end.

FIGURE 8. Evolution of the protrusion profile of a TSV with three grains placed near the top end: (a) $t = 0$, (b) $t = 10000$, (c) $t = 20000$ and (d) $t = 30000$.

symmetries in the TSV geometry, grain structure and loading condition, the deformations in the left and right halves of the TSV occur uniformly and accommodate each other. Hence, the motion of the triple junctions can occur smoothly without impediment.

Fig. 9 shows the relationship between the grain misorientation and the protrusion for the case illustrated in Fig. 1, i.e., the TSV with two grains near the top end. The orientations of grains A and B are systemically studied: the orientation of one grain is varied from 5° to 85°, while that of the other grain remains the same. The results show that the protrusion height increases and then decreases with increasing misorientation. The maximum protrusion height occurs at a misorientation of approximately 60°. The GB formed with this special misorientation is referred to as a twin boundary, which has the lowest mobility and exhibits the highest stability among all the kinds of GBs. A lower mobility means that GB migration and accommodation of the loading applied to the TSV are more difficult. Lacking compliance, the grains are directly pushed out of the TSV surface, thereby resulting in substantial protrusion.

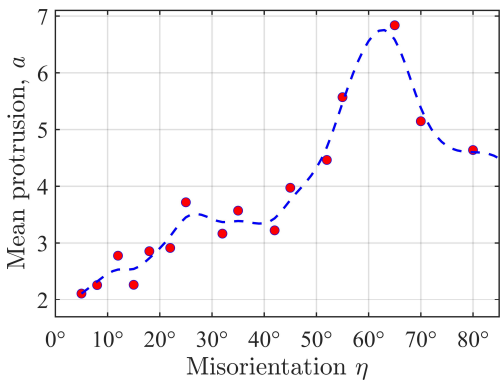

FIGURE 9. Plot of the mean protrusion height versus misorientation. The grain structure and loading condition are defined in Fig. 1a.

D. STRAIN IN TSVS

Fig. 10 shows the distribution of strain components, i.e., ε_{xx}, ε_{yy}, γ_{xy}, and γ_{yx}, at $t = 5000$ for the structure as illustrated in Fig. 1, where two grains are located near the top end. The defect atoms inside the TSV are indicated by black dots. The strain along the GBs is found to be more pronounced than that in the grain interior: the average strains along the GBs are $\bar{\varepsilon}_{xx} \approx -0.25$ and $\bar{\varepsilon}_{yy} \approx -0.25$, while $\bar{\varepsilon}_{xx} \approx 0.025$ and $\bar{\varepsilon}_{yy} \approx 0.034$ in the grain interior, as shown in Figs. 10a-b. The magnitude of the strain along the GBs is approximately 10 times that in the grain interior. When loading is applied to the TSV, the thickness of the GBs decreases because

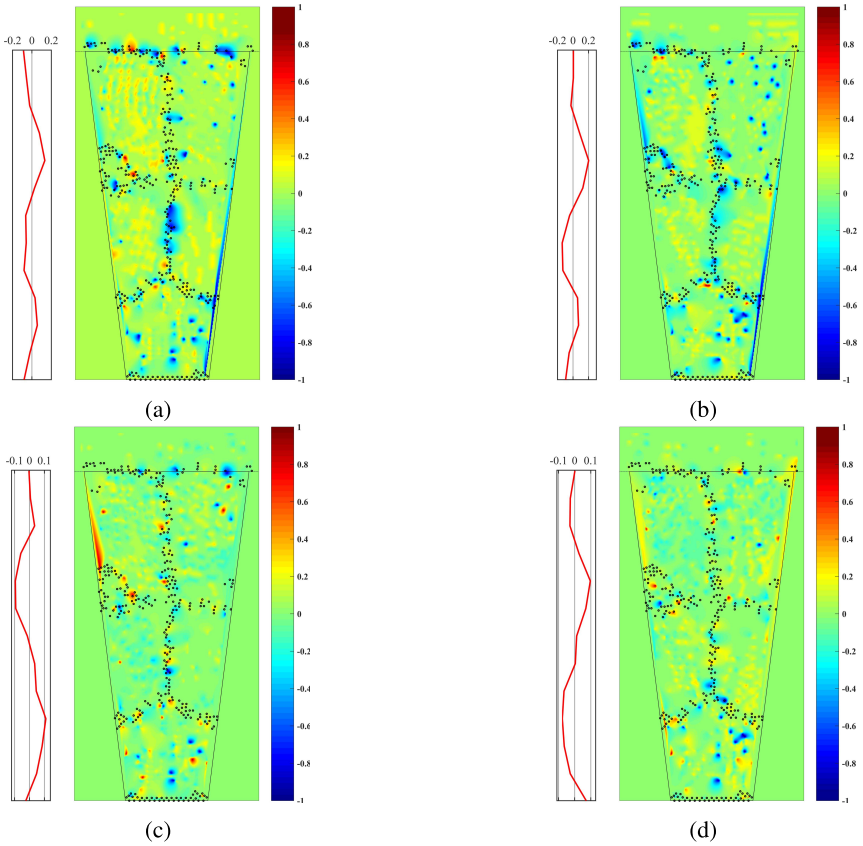

FIGURE 10. Strain distributions of a TSV at $t = 5000$ for the structure as illustrated in Fig. 1, where two grains are located near the top end: (a) ε_{xx}, (b) ε_{yy}, (c) γ_{xy} and (d) γ_{yx}, with the average strain along the y-direction plotted on the left side.

the atoms in the GBs move and become more compact. In addition, the atoms in the GBs move more freely than those in the grain interior, thus leading to a larger deformation along the GBs. Therefore, more pronounced compressive strains are found along the GBs. As shown in Figs. 10c-d, the average shear strains along the GBs and in the grain interior are more or less at similar levels, with $\bar{\gamma}_{xy} \approx 0.007$ and $\bar{\gamma}_{yx} \approx -0.003$ in the grain interior and $\bar{\gamma}_{xy} \approx 0.01$ and $\bar{\gamma}_{yx} \approx -0.001$ along the GBs. The average strain inside the TSV along the y-direction are plotted on the left side of the strain distribution maps in Fig. 10. Note that a point on the curve is the averaged strain over a cross-section of the TSV, i.e., a line in the 2D case, along the x-direction. The average strain curves of ε_{xx} and ε_{yy} exhibit similar distributions. For the shear strains γ_{xy} and γ_{yx}, the two curves almost negate each other.

To further understand the relationship between the strain and protrusion, the principle strains or the eigenstrains in the TSV are calculated. Then, the projection of the eigenstrains onto the y-direction is considered an index to characterize the protrusion tendency. As an example, the eigenstrain projection of the TSV illustrated in Figs. 7a-7b, i.e., the TSV with one grain near the top end, is calculated and plotted in Fig. 11. Two regions, R1 and R2, are marked, and more positive values dominate in region R1, while more negative values dominate in region R2. The projection of the eigenstrains predicts the TSV protrusion behavior: protrusion on the left side and intrusion on the right side of the top surface, which agrees with the final protrusion profile shown in Fig. 7b.

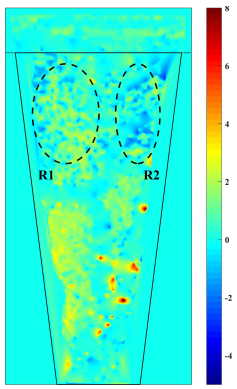

FIGURE 11. Projection of eigenstrains in the TSV shown in Fig. 7a, i.e., the TSV with one grain near the top end, onto the y-direction at $t = 29000$.

IV. CONCLUSION

In this study, the PFC model is used to investigate the effects of temperature, sidewall roughness and grain structure on

the Cu TSV protrusion at the atomic scale. The following conclusions can be drawn:

- A larger protrusion results when the TSV is subjected to a higher temperature. A transition temperature exists at approximately 300°C, at which the deformation mechanism switches from dislocation motion to both diffusional and dislocation creep.
- TSVs with smaller sidewall roughness R_a and wavelength λ_a exhibit a larger protrusion height, in which the role of λ_a is secondary to that of R_a.
- Both protrusion and intrusion can occur in TSVs with the nearest region of the top end fully occupied by a single grain, while the top surface protrudes near both edges when it contains more grains. In TSVs with a symmetric grain structure subjected to symmetric loading, the triple-junction motion and related GB migration can proceed smoothly, thus alleviating protrusion.
- Eigenstrain projection onto the vertical direction can predict the TSV protrusion tendency: regions with positive values contribute to protrusion, while those with negative values contribute to intrusion.

REFERENCES

[1] C.-C. Lee *et al.*, "An overview of the development of a GPU with integrated HBM on silicon interposer," in *Proc. IEEE 66th Electron. Compon. Technol. Conf. (ECTC)*, Las Vegas, NV, USA, May 2016, pp. 1439–1444.

[2] M. M. Shulaker *et al.*, "Three-dimensional integration of nanotechnologies for computing and data storage on a single chip," *Nature*, vol. 547, pp. 74–78, Jul. 2017.

[3] W.-W. Shen and K.-N. Chen, "Three-dimensional integrated circuit (3D IC) key technology: Through-silicon via (TSV)," *Nanoscale Res. Lett.*, vol. 12, no. 1, p. 56, Jan. 2017. [Online]. Available: https://doi.org/10.1186/s11671-017-1831-4

[4] J. P. Gambino, S. A. Adderly, and J. U. Knickerbocker, "An overview of through-silicon-via technology and manufacturing challenges," *Microelectron. Eng.*, vol. 135, pp. 73–106, Mar. 2015. [Online]. Available: http://www.sciencedirect.com/science/article/pii/S0167931714004511

[5] D. Vogel *et al.*, "Stress analyses of high spatial resolution on TSV and BEoL structures," *Microelectron. Rel.*, vol. 54, nos. 9–10, pp. 1963–1968, Sep./Oct. 2014. [Online]. Available: http://www.sciencedirect.com/science/article/pii/S0026271414002947

[6] A. Heryanto *et al.*, "Effect of copper TSV annealing on via protrusion for TSV wafer fabrication," *J. Electron. Mater.*, vol. 41, no. 9, pp. 2533–2542, Sep. 2012. [Online]. Available: https://doi.org/10.1007/s11664–012-2117–3

[7] T. Jiang *et al.*, "Study of stresses and plasticity in through-silicon via structures for 3D interconnects by X-ray micro-beam diffraction," *IEEE Trans. Device Mater. Rel.*, vol. 14, no. 2, pp. 698–703, Jun. 2014.

[8] M. A. Ehsan, Z. Zhou, L. Liu, and Y. Yi, "An analytical through silicon via (TSV) surface roughness model applied to a millimeter wave 3-D IC," *IEEE Trans. Electromagn. Compat.*, vol. 57, no. 4, pp. 815–826, Aug. 2015.

[9] T. Nakamura, H. Kitada, Y. Mizushima, N. Maeda, K. Fujimoto, and T. Ohba, "Comparative study of side-wall roughness effects on leakage currents in through-silicon via interconnects," in *Proc. IEEE Int. 3D Syst. Integr. Conf. (3DIC)*, Jan. 2012, pp. 1–4.

[10] T. Jiang, J. Im, R. Huang, and P. S. Ho, "Through-silicon via stress characteristics and reliability impact on 3D integrated circuits," *MRS Bull.*, vol. 40, no. 3, pp. 248–256, Mar. 2015.

[11] J. D. Messemaeker *et al.*, "Statistical distribution of through-silicon via Cu pumping," *IEEE Trans. Device Mater. Rel.*, vol. 17, no. 3, pp. 549–559, Sep. 2017.

[12] T. Jiang, L. Spinella, J.-H. Im, R. Huang, and P. S. Ho, "Processing effect on via extrusion for TSVs in three-dimensional interconnects: A comparative study," *IEEE Trans. Device Mater. Rel.*, vol. 16, no. 4, pp. 465–469, Dec. 2016.

[13] X. Liu *et al.*, "In-situ microscale through-silicon via strain measurements by synchrotron X-ray microdiffraction exploring the physics behind data interpretation," *Appl. Phys. Lett.*, vol. 105, no. 11, Sep. 2014, Art. no. 112109. [Online]. Available: http://aip.scitation.org/doi/abs/10.1063/1.4896141

[14] C. Okoro *et al.*, "Extraction of the appropriate material property for realistic modeling of through-silicon-vias using μ-Raman spectroscopy," in *Proc. Int. Interconnect Technol. Conf.*, Burlingame, CA, USA, Jun. 2008, pp. 16–18.

[15] J. Liu, Z. Huang, P. P. Conway, F. Altmann, M. Petzold, and F. Naumann, "On reproducing the copper extrusion of through-silicon-vias from the atomic scale," in *Proc. 18th Int. Conf. Electron. Packag. Technol. (ICEPT)*, Harbin, China, Aug. 2017, pp. 789–796.

[16] J. Liu, Z. Huang, Y. Zhang, and P. P. Conway, "Mechanisms of copper protrusion in through-silicon-via structures at the nanoscale," *Jpn. J. Appl. Phys.*, vol. 58, no. 1, Nov. 2018, Art. no. 016502. [Online]. Available: https://doi.org/10.7567%2F1347-4065%2Faae898

[17] J. Liu, Z. Huang, and P. P. Conway, "Linkages between grain structure and protrusion of TSV in 3D packaging," in *Proc. Electron Devices Technol. Manuf. Conf. (EDTM)*, Mar. 2019, pp. 303–305.

[18] K. R. Elder, M. Katakowski, M. Haataja, and M. Grant, "Modeling elasticity in crystal growth," *Phys. Rev. Lett.*, vol. 88, no. 24, Jun. 2002, Art. no. 245701. [Online]. Available: https://link.aps.org/doi/10.1103/PhysRevLett.88.245701

[19] K. R. Elder and M. Grant, "Modeling elastic and plastic deformations in nonequilibrium processing using phase field crystals," *Phys. Rev. E, Stat. Phys. Plasmas Fluids Relat. Interdiscip. Top.*, vol. 70, Nov. 2004, Art. no. 051605. [Online]. Available: https://link.aps.org/doi/10.1103/PhysRevE.70.051605

[20] J. Berry, M. Grant, and K. R. Elder, "Diffusive atomistic dynamics of edge dislocations in two dimensions," *Phys. Rev. E, Stat. Phys. Plasmas Fluids Relat. Interdiscip. Top.*, vol. 73, Mar. 2006, Art. no. 031609. [Online]. Available: https://link.aps.org/doi/10.1103/PhysRevE.73.031609

[21] J. Berry, J. Rottler, C. W. Sinclair, and N. Provatas, "Atomistic study of diffusion-mediated plasticity and creep using phase field crystal methods," *Phys. Rev. B, Condens. Matter*, vol. 92, Oct. 2015, Art. no. 134103. [Online]. Available: https://link.aps.org/doi/10.1103/PhysRevB.92.134103

[22] K. A. Wu, A. Adland, and A. Karma, "Phase-field-crystal model for FCC ordering," *Phys. Rev. E, Stat. Phys. Plasmas Fluids Relat. Interdiscip. Top.*, vol. 81, Jun. 2010, Art. no. 061601. [Online]. Available: https://link.aps.org/doi/10.1103/PhysRevE.81.061601

[23] P. Stefanovic, M. Haataja, and N. Provatas, "Phase field crystal study of deformation and plasticity in nanocrystalline materials," *Phys. Rev. E, Stat. Phys. Plasmas Fluids Relat. Interdiscip. Top.*, vol. 80, Oct. 2009, Art. no. 046107. [Online]. Available: https://link.aps.org/doi/10.1103/PhysRevE.80.046107

[24] T. Jiang *et al.*, "Plasticity mechanism for copper extrusion in through-silicon vias for three-dimensional interconnects," *Appl. Phys. Lett.*, vol. 103, no. 21, Nov. 2013, Art. no. 211906. doi: 10.1063/1.4833020.

[25] J. D. Messemaeker *et al.*, "Correlation between CU microstructure and TSV CU pumping," in *Proc. IEEE 64th Electron. Compon. Technol. Conf. (ECTC)*, Orlando, FL, USA, May 2014, pp. 613–619.

[26] N. Provatas and K. Elder, *Phase-Field Methods in Materials Science and Engineering*, Wiley, Weinheim, Germany, 2011.

[27] A. Stukowski and A. Arsenlis, "On the elastic–plastic decomposition of crystal deformation at the atomic scale," *Model. Simulat. Mater. Sci. Eng.*, vol. 20, no. 3, Mar. 2012, Art. no. 035012. [Online]. Available: https://doi.org/10.1088%2F0965–0393%2F20%2F3%2F035012

[28] A. H. Chokshi, "An analysis of creep deformation in nanocrystalline materials," *Scripta Materialia*, vol. 34, no. 12, pp. 1905–1910, 1996.

[29] M. Kawasaki and T. G. Langdon, "The many facets of deformation mechanism mapping and the application to nanostructured materials," *J. Mater. Res.*, vol. 28, no. 13, pp. 1827–1834, 2013.

[30] L. Chan, M. MacDonald, D. Chung, N. Hutchins, and A. Ooi, "A systematic investigation of roughness height and wavelength in turbulent pipe flow in the transitionally rough regime," *J. Fluid Mech.*, vol. 771, p. 743–777, Apr. 2015.